Research Square

Preprints are preliminary reports that have not undergone peer review.
They should not be considered conclusive, used to inform clinical practice,
or referenced by the media as validated information.

B-Site $(Cr_{0.5}Ta_{0.5})^{4+}$ Substitution Regulating Low-Temperature Sintering and Microwave Dielectric Properties of $Sm_2Zr_3(MoO_4)_9$ Ceramics

Jialin Wu
Taiyuan University of Science and Technology
Yuan-Bin Chen
n2890103@outlook.com

Taiyuan University of Science and Technology
Yeong-Long Chen
Zhaoqing University

Research Article

Keywords: $Sm_2[Zr_{1-x}(Cr_{0.5}Ta_{0.5})_x]_3[MoO_4]_9$ ceramics, low-temperature sintering, ultra-low dielectric loss, Raman spectroscopy, microwave dielectric properties

Posted Date: November 24th, 2026

DOI: https://doi.org/10.21203/rs.3.rs-11725384/v1

License: This work is licensed under a Creative Commons Attribution 4.0 International License.
Read Full License

Additional Declarations: No competing interests reported.

B-Site $(Cr_{0.5}Ta_{0.5})^{4+}$ Substitution Regulating Low-Temperature Sintering and Microwave Dielectric Properties of $Sm_2Zr_3(MoO_4)_9$ Ceramics

Jialin Wu[a], Yuan-Bin Chen*[,a], Yeong-Long Chen[b]

[a] School of electronic information engineering,Taiyuan University of Science and Technology, Taiyuan 030024, Shanxi, PR China

[b]Interdisciplinary and Innovation Research Center, School of Economics and Management, Zhaoqing University, Guangdong, PR China

Abstract

$Sm_2[Zr_{1-x}(Cr_{0.5}Ta_{0.5})_x]_3(MoO_4)_9$ series microwave dielectric ceramics were fabricated via the conventional solid-state reaction route, and the regulation effects of Cr^{3+}/Ta^{5+} co-substitution on phase composition, microstructure, sintering behavior, bonding characteristics and microwave dielectric properties were systematically investigated. The calculated ionicity fractions of different chemical bonds follow the sequence: Sm–O (85.0%) > (Cr/Ta)–O (79.2%) > Mo–O (72.5%). As the doping level x increases, the ionicity fractions of both Mo–O and (Cr/Ta)–O bonds decrease synchronously, accompanied by a gradual reduction in permittivity (ε_r). According to the ionicity-polarizability mechanism, the attenuation of bond ionicity leads to the decline of intrinsic polarizability, which further causes ε_r to drop from 10.52 to 7.23, while the variation of relative density exerts a synergistic effect in this process. The Mo–O bond contributes approximately 71.2% of the total lattice energy (U_β) and acts as the core factor determining the lattice rigidity of the system. When x = 0.05, the U_β of Mo–O bond reaches its minimum value of ~261.6 kJ/mol; when $x \geq 0.08$, U_β rebounds to ~264.1 kJ/mol, but the intensified phonon scattering effect degrades the Q×f value from 72764 GHz to 13417 GHz. This evolution trend is highly consistent with the broadening behavior of Raman full width at half maximum (FWHM), confirming that the dielectric loss of the system is dominated by the phonon scattering mechanism. The temperature coefficient of resonant frequency (τ_f) of the system shows a negative correlation with Mo–O bond energy: a higher bond energy (~603.6 kJ/mol) makes τ_f closer to zero (–27.26 ppm/°C), while a lower bond energy (~595.4

kJ/mol) leads to a more negative τf (–43.08 ppm/°C), indicating that stronger Mo–O bonds can suppress anharmonic vibrations and significantly improve the temperature stability of the material.

***Corresponding author: Yuan-Bin Chen， E-mail address: n2890103@outlook.com**

Keywords: $Sm_2[Zr_{1-x}(Cr_{0.5}Ta_{0.5})_x]_3[MoO_4]_9$ ceramics; low-temperature sintering; ultra-low dielectric loss; Raman spectroscopy; microwave dielectric properties

1. Introduction

With the large-scale deployment of fifth-generation (5G) mobile communication technology and the accelerating vision of sixth-generation (6G) networks, wireless systems are rapidly evolving toward higher frequency bands, lower latency, and greater integration density. In this context, microwave dielectric ceramics, as core materials for critical radio frequency components such as filters, resonators, and antenna substrates, are facing increasingly stringent performance requirements [1-3]. To meet the demands of future high-speed data transmission, dielectric materials must synergistically possess a moderate dielectric constant (ε_r) to minimize signal propagation delay, an ultra-high quality factor (Q×f, i.e., low dielectric loss) to ensure signal integrity, and a near-zero temperature coefficient of resonant frequency (τ_f) to guarantee frequency stability over a wide temperature range [4, 5].

Low-temperature co-fired ceramics (LTCC) technology, as a key enabler for miniaturization and three-dimensional integration of radio-frequency modules, requires materials that can be co-fired with low-melting-point metal electrodes such as silver and copper at temperatures below 960 °C [6-9]. Consequently, exploring novel ceramic systems that simultaneously exhibit excellent microwave dielectric properties and low sintering temperatures has become a central research focus in the field of electronic materials. In recent years, molybdate-based ceramics have attracted considerable attention due to their intrinsically low sintering temperatures, tunable crystal structures, and favorable dielectric properties [10-15]. Among them, the rare-earth zirconium molybdate system $Ln_2Zr_3(MoO_4)_9$ (Ln = La, Ce, Pr, Nd, Sm, Eu, Gd), which crystallizes in a trigonal structure with space group $R\bar{3}c$, has demonstrated

remarkable application potential, with its inherently low sintering temperature (typically below 800 °C) providing a natural advantage for LTCC applications [16-21].

However, the dielectric loss of single-phase $Ln_2Zr_3(MoO_4)_9$ ceramics remains insufficient to fully satisfy the stringent ultra-low-loss requirements of 5G/6G communications. To overcome this bottleneck, chemical substitution strategies have proven to be effective approaches for optimizing microwave dielectric properties, including single-ion doping, isovalent/heterovalent substitution, and complex-ion co-substitution [22, 23]. Recent studies have demonstrated that introducing highly polarizable complex ions such as $(Bi_{0.5}Ta_{0.5})^{4+}$ at the Zr^{4+} site can significantly enhance the quality factor of the $Ce_2Zr_3(MoO_4)_9$ system [24, 25]. Inspired by this, our group previously conducted a systematic investigation on the $Nd_2[Zr_{1-x}(Bi_{0.5}Ta_{0.5})_x]_3(MoO_4)_9$ system, confirming that B-site complex substitution can effectively increase lattice rigidity, suppress phonon scattering, and thus achieve a substantial improvement in Q×f values at a sintering temperature of 750 °C. Nevertheless, further reducing the sintering temperature while optimizing thermal stability remains a critical challenge for advancing these materials toward practical applications.

Building upon this foundation, the present study proposes a novel "B-site complex-ion substitution" strategy, employing $(Cr_{0.5}Ta_{0.5})^{4+}$ as the substituent group to modify the $Sm_2Zr_3(MoO_4)_9$ matrix. This design is motivated by the following considerations: (1) Sm^{3+}, possessing a smaller ionic radius and higher bond strength compared to Nd^{3+}, is expected to enhance lattice stability and reduce intrinsic loss; (2) the incorporation of Cr^{3+} may modulate the local crystal field and the distortion degree of oxygen octahedra, thereby tuning the polarization behavior; (3) the $(Cr_{0.5}Ta_{0.5})^{4+}$ complex ion exhibits good size compatibility with Zr^{4+}, facilitating the formation of continuous solid solutions and potentially further suppressing dielectric loss through enhanced lattice energy. The core objective of this study is to achieve microwave dielectric ceramics with simultaneously high Q×f values, moderate ε_r, and near-zero τf at sintering temperatures below 750 °C through precise control of the substitution

content x, while systematically elucidating the structure–property correlation mechanisms.

As presented in Table 1, a series of $Ln_2Zr_3(MoO_4)_9$ (Ln = La, Ce, Pr, Nd, Sm, Eu, Gd) ceramics were systematically evaluated for their microwave dielectric properties in this work. The results demonstrate that the selection of rare-earth ions exerts a pronounced effect on the dielectric performance. Compared with the previously reported $Ce_2[Zr_{1-x}(Bi_{1/2}Ta_{1/2})_x]_3(MoO_4)_9$ ceramics, the Sm-substituted composition exhibits a substantial improvement in the Q×f value. This performance enhancement is primarily attributed to the smaller ionic radius and stronger bonding strength of Sm^{3+} relative to Ce^{3+}, which facilitates the formation of a more compact and stable crystal structure, thereby effectively reducing the dielectric loss.

To this end, a series of $Sm_2[Zr_{1-x}(Cr_{0.5}Ta_{0.5})_x]_3(MoO_4)_9$ ($0.02 \le x \le 0.11$) ceramics were synthesized via the conventional solid-state reaction method. The effects of substitution content on phase composition, lattice parameters, microstructure, and phonon vibrational modes were systematically characterized using X-ray diffraction (XRD) coupled with Rietveld refinement, scanning electron microscopy (SEM), and Raman spectroscopy. Importantly, the P-V-L complex chemical bond theory will be employed to quantitatively calculate the ionicity (f_i), lattice energy (U), bond energy (E), and linear thermal expansion coefficient (α_L) of individual chemical bonds, thereby elucidating the intrinsic contributions of these bond parameters to ε_r, Q×f, and τ_f. Finally, the co-firing compatibility of this material system with Ag electrodes will be evaluated to verify its practical potential for LTCC processing. This study is expected to provide a new material candidate and theoretical guidance for the development of ultra-low-loss, low-temperature-sintered microwave dielectric ceramics for next-generation wireless communication systems.

2 Experimental procedure

In this work, a conventional solid-state reaction route was adopted for the synthesis of $Sm_2[Zr_{1-x}(Cr_{0.5}Ta_{0.5})_x]_3[MoO_4]_9$ (x = 0.02–0.11) ceramic powders, utilizing high-purity Sm_2O_3 (99.9%, Macklin), ZrO_2 (99.9%, Aladdin), Cr_2O_3 (99.5%, Aladdin), Ta_2O_5 (99%, Macklin), and MoO_3 (99.9%, Aladdin) as the raw materials.

Stoichiometric amounts of these reagents were first blended and then subjected to wet ball-milling in deionized water with zirconia grinding media for a duration of 24 h to ensure compositional homogeneity. Following milling, the resulting slurries were dehydrated at 95 °C, and the dried mixtures were subsequently calcined at 675 °C for 2 h in an alumina boat to initiate the primary solid-state reaction. After calcination, the products were finely ground and re-milled for another 20 h to achieve a uniform particle size distribution. The obtained powders were then combined with polyvinyl alcohol (PVA, ~12 wt%) as a temporary binder, thoroughly granulated, and compacted into cylindrical green bodies (11 mm in diameter and 6 mm in height) under a uniaxial pressure of 100 MPa. Densification of these compacts was finally accomplished by sintering in air for 4 h within a temperature window of 725–825 °C.

Phase purity and crystal structure of the as-sintered samples were examined via X-ray diffraction (XRD) on a Rigaku SmartLab Studio II diffractometer equipped with Cu Kα radiation (λ = 1.5406 Å), with data collected across a 2θ range of 10°–80°. Lattice parameters and other structural details were extracted through Rietveld refinement using the GSAS-II software package. For microstructural observation, the sintered pellets were sequentially ground and polished to a scratch-free surface using diamond abrasives down to 0.35 μm, followed by thermal etching at a temperature 50 °C below the respective sintering temperature for 20 min to expose clear grain boundaries. A Zeiss Sigma 360 VP field-emission scanning electron microscope (FE-SEM) coupled with an energy-dispersive X-ray spectrometer (EDS) was employed to inspect the surface morphology and elemental dispersion. Grain size statistics were derived from SEM micrographs via the linear intercept method, as implemented in ImageJ software, in accordance with ASTM E112 standards.

Microwave dielectric characterization was performed on an Anritsu MS4640B vector network analyzer, with the $TE_{01}\delta$ and TE_{011} resonant modes selected as per the established Hakki–Coleman and Courtney [26] procedures, to determine the relative permittivity (ε_r) and the unloaded quality factor (Q×f). The resonant frequency temperature coefficient (τf) was evaluated by monitoring the frequency shift between 25 °C and 85 °C within a thermostatically controlled cavity, and was computed using

Equation (1):

$$\tau_f = \frac{f_{\mathrm{T}} - f_{\mathrm{t}}}{f_{\mathrm{t}}(T - \mathrm{t})}(\mathrm{ppm/℃}) \qquad (1)$$

, where f_{25} and f_{85} represent the measured resonant frequencies at 25 °C and 85 °C, respectively. Densities of the fired ceramics were measured using the Archimedes immersion technique with a balance readable to ±0.001 g, and the relative density ($\rho_{relative}$) was subsequently derived by comparing the experimental bulk density against the theoretical X-ray density. Additionally, Raman scattering spectra were acquired at ambient conditions on a LabRAM HR Evolution spectrometer, using a 532 nm laser as the excitation source, over a spectral window of 100–1200 cm^{-1}, so as to probe the intrinsic lattice vibrational modes and to establish their correlation with the observed dielectric behavior.

$$\rho_{\mathrm{density}} = \frac{\rho_{\mathrm{water}}\mathrm{m}}{\Delta\mathrm{m}} \qquad (2)$$

The parameter $\rho_{density}$ is the bulk density derived from measurements, with ρwater being the water density, m the mass measured in air, and Δm the mass discrepancy introduced by submersion, calculated as the air mass minus the immersed mass.

The crystallographic density (ρ_{tho}) is given by the following relationship:

$$\rho_{\mathrm{tho}} = \frac{\mathrm{MZ}}{\mathrm{V_{ce}N_A}} \qquad (3)$$

In the above formula, ρ_{tho} denotes the theoretical density of the as-synthesized ceramic, while M, Z, NA, and V_{cell} correspond to the molar mass of the target compound, the number of formula units contained in a single unit cell, Avogadro's constant, and the refined unit cell volume of the sample, respectively. On this basis, the relative density ($\rho_{relative}$) of the sintered specimens can be further derived via the following equation:

$$\rho_{\text{relative}}(\%) = \frac{\rho_{\text{density}}}{\rho_{\text{tho}}} \times 100 \quad (4)$$

ρ_{re} represents the relative density.

3 Results and discussion

3.1 XRD and Crystal Structure Analysis

The phase purity and crystallographic evolution of $Sm_2[Zr_{1-x}(Cr_{0.5}Ta_{0.5})_x]_3[MoO_4]_9$ ($0.02 \leq x \leq 0.11$) solid solutions, sintered at 800 °C, were first examined via X-ray diffraction, with the corresponding patterns presented in Fig. 1(a). All observed reflections were unequivocally indexed to the rhombohedral $Sm_2Zr_3(MoO_4)_9$ prototype (PDF#04-012-7342) [16], and the complete absence of extraneous peaks firmly established the phase-pure nature of the as-prepared specimens. Structure refinement against the diffraction data was subsequently undertaken utilizing the Rietveld algorithm [27] as embedded in the GSAS-II package, with initial structural parameters derived from CIF data sourced from the FindIt repository. As the substitution content of $(Cr_{0.5}Ta_{0.5})^{4+}$ increases, the diffraction peaks in the 2θ range of 22°–24° exhibit a progressive shift toward higher angles, as illustrated in Fig. 1(b). In contrast, Fig. 1(c) reveals that the unit-cell volume gradually contracts with increasing $(Cr_{0.5}Ta_{0.5})^{4+}$ doping level. Such monotonic contraction can be rationalized by the size effect, given that the mixed $(Cr_{0.5}Ta_{0.5})^{4+}$ octahedral species possesses an effective ionic radius of 0.6275 Å (sixfold coordination, where $r(Cr^{3+})$ = 0.615 Å and $r(Ta^{5+})$ = 0.64 Å), which is appreciably smaller than that of the native Zr^{4+} ion (0.72 Å). This steric consideration is further supported by the refined bond length variations itemized in Table 4, hinting at consequential alterations in the microstructural arrangement and concomitant dielectric properties. Figure 1 (d) shows no secondary impurity phases are detected in the XRD patterns of the co-fired samples, confirming that no significant chemical reaction occurs between $Sm_2[Zr_{1-x}(Cr_{0.5}Ta_{0.5})_x]_3(MoO_4)_9$ ceramics and Ag at 800 °C, and the two components exhibit excellent chemical co-firing compatibility. This result demonstrates that the series of ceramics possesses extremely high phase stability with silver electrodes under low-temperature sintering conditions, fully meeting the electrode co-firing application requirements of low-temperature co-fired ceramic

(LTCC) devices.

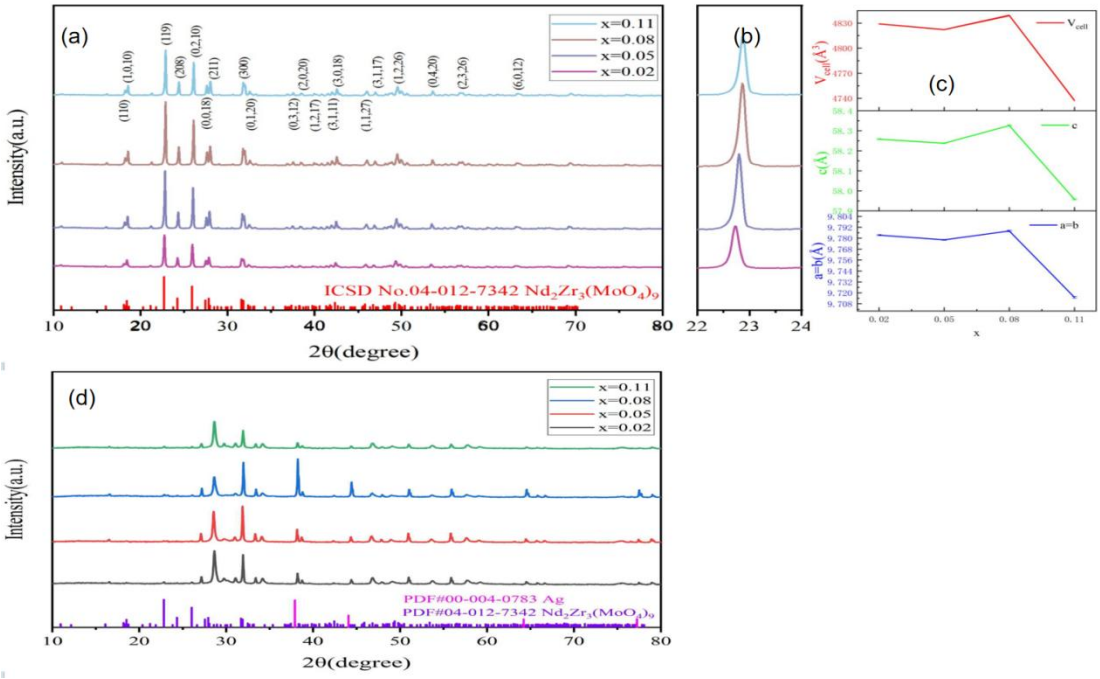


Fig 1. (a) XRD patterns of $Sm_2[Zr_{1-x}(Cr_{0.5}Ta_{0.5})_x]_3[MoO_4]_9$ ceramics with x = 0.02–0.11 sintered at the optimal temperature of 800 °C; (b) the reflections located between 22° and 24° (2θ), (c) the volume change as a function of the substitution fraction x, (d) XRD patterns of $Sm_2[Zr_{1-x}(Cr_{0.5}Ta_{0.5})_x]_3(MoO_4)_9$ ceramics co-fired with silver powder at 800 °C for 2h.

For completeness, a three-dimensional polyhedral representation of the parent $Sm_2Zr_3(MoO_4)_9$ framework, together with its local coordination environments, is supplied as Fig. 2(e) (reproduced with reference to [25, 27]). Additionally, the phase stability across the substitution series was confirmed, retaining the single rhombohedral phase without any trace of secondary crystallization or structural transformation over the entire doping interval explored [27].

Fig. 2(a)–(d) display the Rietveld refinement XRD patterns of $Sm_2[Zr_{1-x}(Cr_{0.5}Ta_{0.5})_x]_3[MoO_4]_9$ ceramics with varying substitution levels (x = 0.02–0.11) sintered at 800 °C. All diffraction peaks are well indexed to the standard pattern of $Sm_2Zr_3(MoO_4)_9$ (PDF#04-012-7342), with no detectable secondary phases, confirming the formation of a single-phase structure with rhombohedral symmetry (space group $R\bar{3}c$, No. 167). Rietveld structure refinement was carried out using the CIF file retrieved from the FindIt crystal database via the GSAS-II software package.

The refinement results of representative specimens, as presented in Fig. 2(a)–(d), show an excellent consistency between the experimental and calculated diffraction patterns. The refinement indicators Rwp and χ^2 fall within the reliable fitting range, which fully validates the accuracy of the adopted structural model. The refined lattice parameters are summarized in Table 2. Fig. 2(e) displays the refined crystal structure schematic of the $Sm_2[Zr_{1-x}(Cr_{0.5}Ta_{0.5})_x]_3[MoO_4]_9$ ceramics obtained through Rietveld analysis of XRD patterns. In the depicted structure, Sm^{3+} cations are coordinated with nine oxygen anions, forming a fourteen-faced polyhedron (tetradecahedron). Zr^{4+} and the substituting $(Cr_{0.5}Ta_{0.5})^{4+}$ ions occupy octahedral sites coordinated by six oxygen atoms, while Mo^{6+} ions are tetrahedrally coordinated with four oxygen atoms, giving rise to MoO_4 tetrahedral units. A detailed examination of the refinement results listed in Table 2 indicates that the reliability factors of the Rietveld refinements fall within acceptable ranges: Rwp = 9.369%–10.906%, Rp = 6.69%–8.23%, and χ^2 = 1.66–2.08. These values satisfy the widely adopted refinement-quality criteria, as exemplified in reference [27]. Moreover, the refined lattice parameters compiled in Table 2 and bond lengths in Table 4 consistently show an overall contraction of the lattice parameters and unit-cell volume (V) with increasing substitution level x, a trend that aligns well with the peak-shift behavior observed in the XRD patterns (Fig. 1(a, b)).

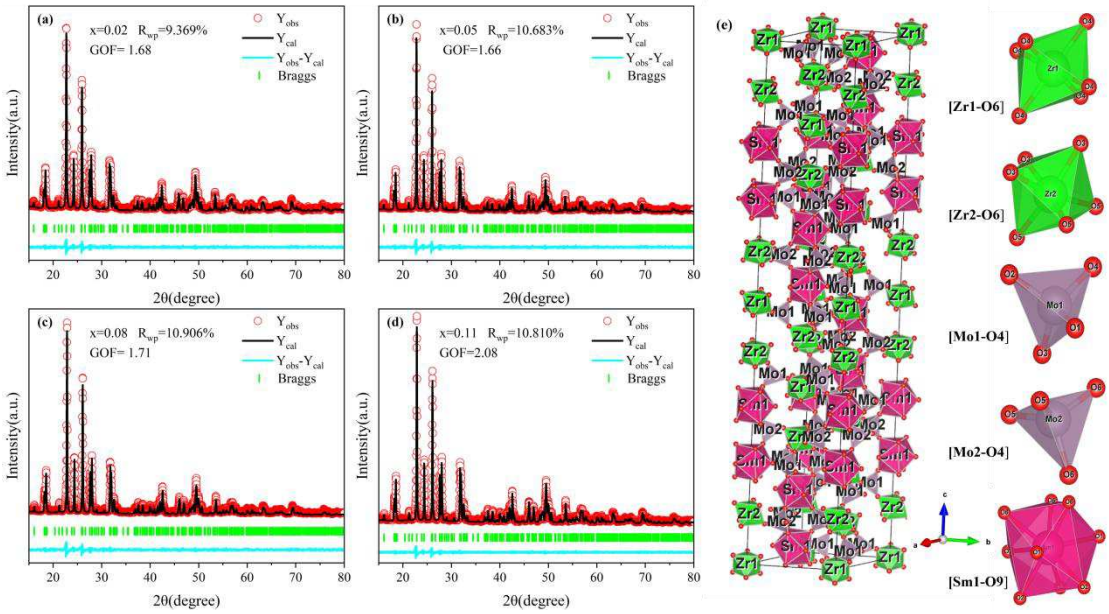


Fig. 2. (a–d) Rietveld refinement XRD patterns of $Sm_2[Zr_{1-x}(Cr_{0.5}Ta_{0.5})_x]_3[MoO_4]_9$ (x = 0.02, 0.05, 0.08, 0.11) ceramics. (e) Crystal structure schematic and coordination polyhedra ([Sm1-O9],

[Zr1-O6], [Mo1-O4], [Mo2-O4]).

Table 1 Comparison of microwave dielectric properties of molybdate system ceramic.

Ceramics	S.T.(℃)	ε_r	Qxf (GHz)	τ_f (ppm/℃)	Reference
$Nd_2Zr_3(MoO_4)_9$	850	10.8	58,942	-40.9	[16]
$Ce_2Zr_3(MoO_4)_9$	575	10.69	19,062	-1.29	[17]
$La_2Zr_3(MoO_4)_9$	775	10.8	50,628	-38.8	[18]
$Pr_2Zr_3(MoO_4)_9$	650	10.72	64,200	-13	[20]
$Ce_2[Zr_{1-x}(Al_{1/2}Ta_{1/2})_x]_3(MoO_4)_9$	850	10.46	8,376	-11.5	[25]
$Pr_2Zr_3(Mo_{0.94}W_{0.06}O_4)_9$	825	9.82	61,892	-8.84	[20]
$(La_{0.2}Nd_{0.2}Sm_{0.2}Eu_{0.2}Gd_{0.2})_2Zr_3(MoO_4)_9$	750	10.46	59,713	-21.94	[22]
$Sm_2[Zr_{1-x}(Cr_{0.5}Ta_{0.5})_x]_3[MoO_4]_9$	800	10.52	72,764	-32.59	This work

Table 2 Lattice parameters, unit cell volume, and refinement parameters of $Sm_2[Zr_{1-x}(Cr_{0.5}Ta_{0.5})_x]_3[MoO_4]_9$ ceramics.

$Sm_2[Zr_{1-x}(Cr_{0.5}Ta_{0.5})_x]_3[MoO_4]_9$	V(Å3)	α=β(°)	γ (°)	Rp(%)	Rwp(%)	χ2
x=0.02	4829.1	90	120	6.69	9.369	1.68
x=0.05	4822.3	90	120	7.89	10.683	1.66
x=0.08	4839.2	90	120	8.23	10.906	1.71
x=0.11	4737.3	90	120	7.96	10.810	2.08

3.2 SEM and Average Grain Size Analysis

Fig. 3 displays representative SEM images of thermally etched surfaces for $Sm_2[Zr_{1-x}(Cr_{0.5}Ta_{0.5})_x]_3[MoO_4]_9$ ceramics with varying x values (0.02, 0.05, 0.08, and 0.11) sintered at 800 °C. The microstructures, revealed after standard polishing and thermal etching procedures, exhibit distinct grain boundaries and variable porosity levels. As the dopant concentration x rises, a clear trade-off emerges: grain size progressively increases from 1.585 μm (x = 0.02) to 4.084 μm (x = 0.11), while the relative density concurrently decreases from 96.82% to 84.85%. The low-x composition (x = 0.02) is characterized by fine equiaxed grains and high density, whereas the high-x counterpart (x = 0.11) presents coarse faceted grains accompanied

by pronounced porosity and reduced densification. Collectively, these observations suggest that although elevated $(Cr_{0.5}Ta_{0.5})^{4+}$ incorporation accelerates grain coarsening, it simultaneously degrades the sinterability and overall compactness of the material.

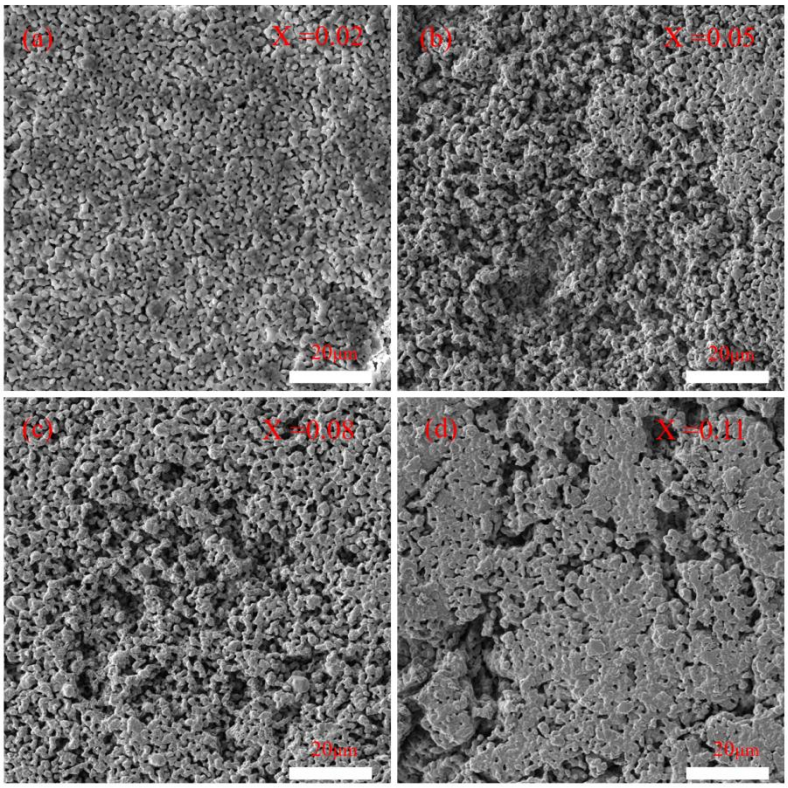


Figure 3. SEM micrographs of $Sm_2[Zr_{1-x}(Cr_{0.5}Ta_{0.5})_x]_3[MoO_4]_9$ ceramics sintered at 800 ℃: (a) x = 0.02, (b) x = 0.05, (c) x = 0.08, (d) x = 0.11.

Fig. 4(a–d) presents the SEM micrographs of $Sm_2[Zr_{0.98}(Cr_{0.5}Ta_{0.5})_{0.02}]_3[MoO_4]_9$ ceramics sintered at various temperatures ranging from 725 to 825 °C. In the low-temperature range of 725–750 °C (Fig. 4(a, b)), the samples exhibit pronounced intergranular porosity. Such pores originate from insufficient thermal activation during sintering, which impedes complete grain coalescence and leaves distinct voids along the grain boundaries. Upon elevating the temperature to the optimized level of 800 °C (Fig. 4(c)), a dense microstructure is attained, characterized by well-developed grains and tightly bonded grain interfaces with minimal observable pores. Under this

sintering condition, the relative density, dielectric constant, and Q×f value all reach their maximum levels. However, further increasing the temperature to 825 °C (Fig. 4(d)) triggers abnormal grain growth, with grain coarsening leading to intergranular cracking or thermal voiding, which is known to be detrimental to the material's overall performance [28–30].

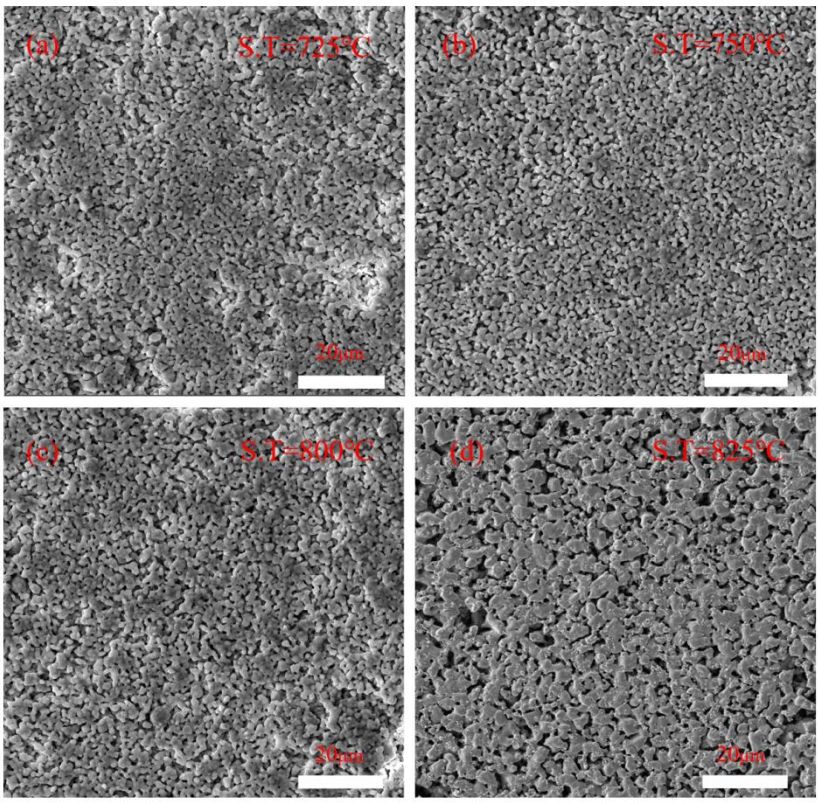


Figure 4. SEM micrographs of $Sm_2[Zr_{0.98}(Cr_{0.5}Ta_{0.5})_{0.02}]_3[MoO_4]_9$ ceramics sintered at various temperatures.

The grain size statistical distributions corresponding to the various compositions are depicted in Fig. 5. With increasing substitution fraction x, the average grain size shifts toward higher values, confirming the grain growth promotion effect of $(Cr_{0.5}Ta_{0.5})^{4+}$ co-substitution. Meanwhile, the apparent density and densification behavior as a function of sintering temperature are illustrated in Fig. 7(a). As the sintering temperature rises from 725 to 800 °C, progressive densification is observed, achieving the maximum relative density of 96.82% at 800 °C. Beyond 800 °C, the relative density declines due to oversintering and pore growth.

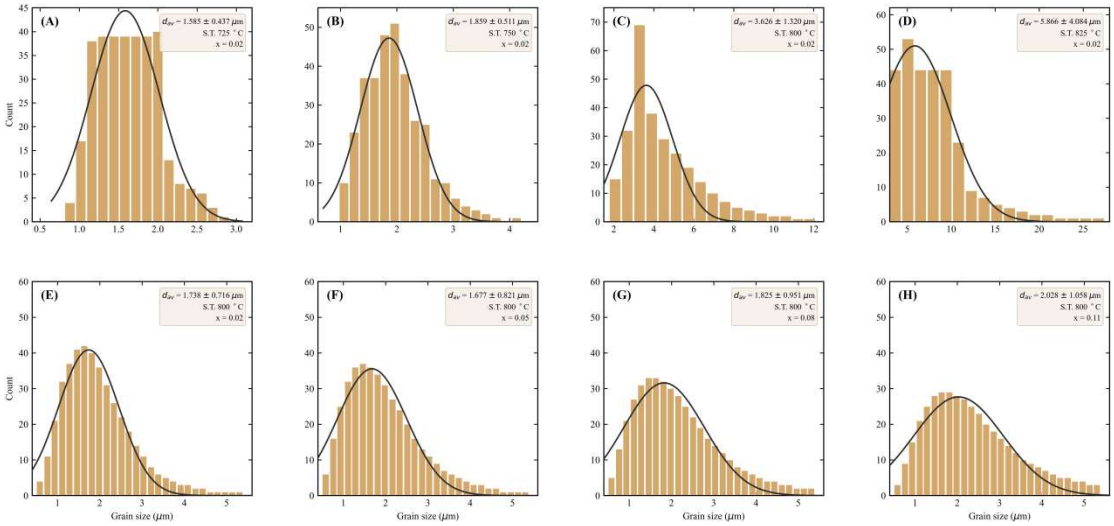


Fig. 5. Grain size distribution histograms of $Sm_2[Zr_{1-x}(Cr_{0.5}Ta_{0.5})_x]_3[MoO_4]_9$ ceramics (A-E) x = 0.02, (F) x = 0.05, (G) x = 0.08, and (H) x = 0.11.

Fig. 6 presents the EDS elemental mapping and compositional spectrum of the $Sm_2[Zr_{0.98}(Cr_{0.5}Ta_{0.5})_{0.02}]_3[MoO_4]_9$ ceramic sintered at 800 °C. It can be observed that the atomic ratios of Sm, Zr, Cr, Ta, Mo, and O are in general agreement with the nominal stoichiometric molar ratios of $Sm_2[Zr_{0.98}(Cr_{0.5}Ta_{0.5})_{0.02}]_3[MoO_4]_9$ ceramics. The slight deviations may be attributed to instrumental sensitivity and background calibration inherent to the EDS technique. Therefore, the successful formation of the target solid solution phase without elemental segregation is confirmed.

In the sintering temperature range of 725–775 °C, the ceramic samples exhibited a relatively high residual porosity. The optimal densification was achieved at 800 °C, with a maximum relative density of 96.82% (as shown in Fig. 7(a)). However, when the sintering temperature exceeded 800 °C, excessive grain coarsening occurred,

which in turn induced the formation of intergranular pores and consequently led to a reduction in relative density. The bulk density and relative density evolution of $Sm_2[Zr_{1-x}(Cr_{0.5}Ta_{0.5})_x]_3[MoO_4]_9$ ceramics thermally treated at sintering temperatures spanning 725 °C to 825 °C are plotted in Fig. 7(a). The relative density exhibits a non-monotonic variation: it progressively rises with elevated temperature, peaks at 800 °C, and subsequently undergoes a gradual reduction. This finding offers solid experimental support for the SEM morphological observations, firmly identifying 800 °C as the most favorable sintering temperature to attain optimal densification for this ceramic system.

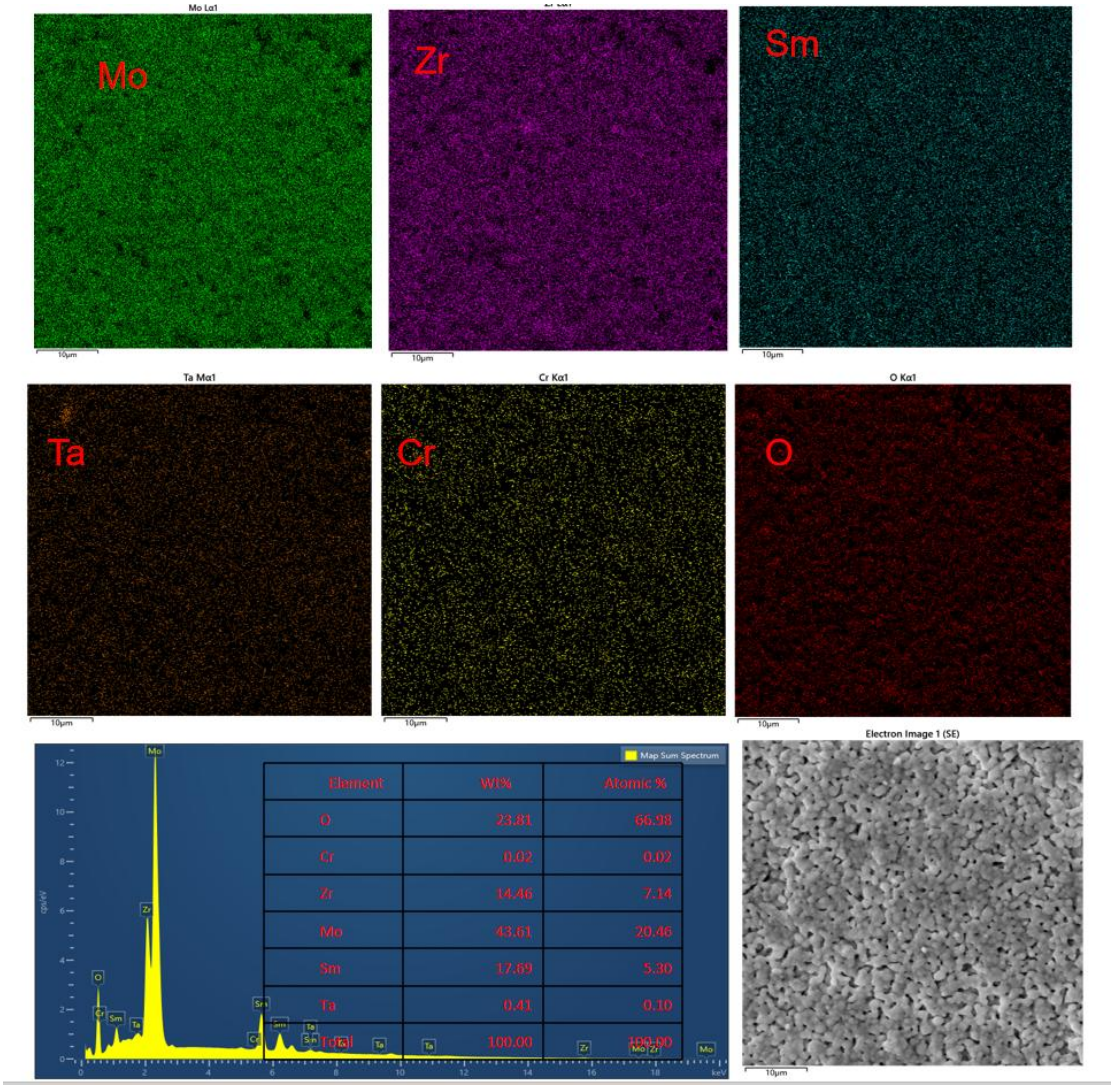


Fig. 6. EDS elemental mapping and energy spectrum of $Sm_2[Zr_{0.98}(Cr_{0.5}Ta_{0.5})_{0.02}]_3[MoO_4]_9$ ceramic sintered at 800 °C.

Fig. 7(b–d) systematically illustrates how the three key microwave dielectric parameters, i.e., dielectric constant (ε_r), quality factor multiplied by resonant frequency (Q×f), and temperature coefficient of resonant frequency (τf), evolve as a function of sintering temperature. It is noteworthy that the variation profiles of ε_r and Q×f follow almost identical tendencies with the relative density curve, reaching optimal values of 10.52 and 72,764 GHz synchronously at 800 °C for x = 0.02. Such a strong correlation convincingly verifies that the densification level acts as one of the dominant extrinsic determinants governing the overall microwave dielectric performance. In contrast, the τf value fluctuates within a moderate window from –43.08 ppm/°C to –27.26 ppm/°C, demonstrating that the sintering temperature and substitution content collectively tune the temperature stability of the as-prepared $Sm_2[Zr_{1-x}(Cr_{0.5}Ta_{0.5})_x]_3[MoO_4]_9$ ceramics.

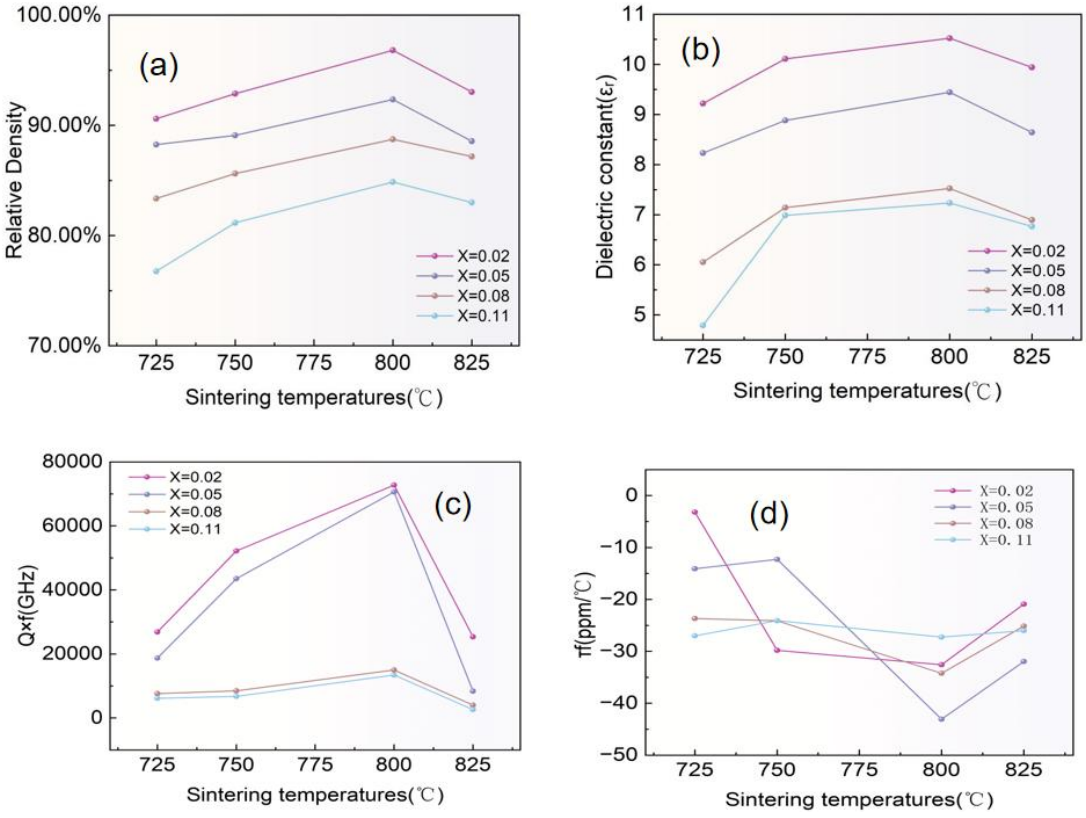


Fig. 7. Microwave dielectric properties and densification of $Sm_2[Zr_{1-x}(Cr_{0.5}Ta_{0.5})_x]_3[MoO_4]_9$ ceramics as a function of sintering temperature: (a) relative density, (b) dielectric constant (εr), (c) quality factor (Q×f), and (d) temperature coefficient of resonant frequency (τf).

The microwave dielectric constant (εr) is governed by both extrinsic and intrinsic factors. Extrinsic contributions arise from secondary phases and relative density (porosity), whereas intrinsic ones are associated with crystal structure, ionic polarizability, and bond ionicity [31, 32]. Fig. 7(b) depicts the temperature-dependent variation of εr for samples over the sintering range of 725–825 °C. All curves exhibit a consistent trend: εr increases with temperature up to 800 °C and then declines beyond this point, reaching a maximum value of 10.52 at 800 °C for x = 0.02. Notably, the relative density of $Sm_2[Zr_{1-x}(Cr_{0.5}Ta_{0.5})_x]_3[MoO_4]_9$ follows a nearly identical evolution (Fig. 7(a)), implying that densification directly modulates the effective dielectric response in the microwave regime. Meanwhile, at the fixed sintering temperature of 800 °C, as the $(Cr_{0.5}Ta_{0.5})^{4+}$ substitution level increases, the relative density decreases from 96.82% to 84.85% (Table 3), contributing to the progressive decrease of ε_r.

Table 3 Dielectric properties, theoretical polarizabilities, density, and Mo–O bond parameters of $Sm_2[Zr_{1-x}(Cr_{0.5}Ta_{0.5})_x]_3[MoO_4]_9$ (x = 0.02–0.11) ceramics sintered at 800 °C.

Substitution content (x)	0.02	0.05	0.08	0.11
Q×f (GHz)	72,764	70,624	15,016	13,417
εr	10.52	9.44	7.52	7.23
τ_f (ppm/°C)	-32.59	-43.08	-34.22	-27.26
ε_{rtheo}	6.11	6.13	6.08	6.39
α_{theo} (Å^3)[per cell, Z=6]	726.6024	726.5160	726.4296	726.3432
α_{theo}/Vm	0.1505	0.1507	0.1501	0.1533
ρ_{theo} (g/cm^3)	4.158	4.169	4.159	4.253
Relative density (%)	96.82	92.35	88.72	84.85
E(Mo–O) (kJ/mol)	596.77	595.38	603.59	603.10
fi(Mo–O)	0.7253	0.7258	0.7232	0.7233

To quantitatively evaluate the porosity effect on the dielectric constant, the porosity-corrected permittivity (ε_{corr}) was calculated using the following equations [32]:

$$P=1-\rho_{re}=1-\frac{\rho_{desity}}{\rho_{th}} \quad (5)$$

$$\varepsilon_{corr}=\varepsilon_r\left(1+\frac{3}{2}P\right) \quad (6)$$

The calculated values of ε_{corr}, P, and ρ_{re} are compiled in Table 3. It is evident that εcorr consistently exceeds the measured εr across all compositions, confirming that the presence of porosity exerts a degrading influence on the dielectric constant [33, 34].

To elucidate the microscopic origin of polarization behavior in the present Sm-based molybdate ceramic system, the intrinsic ionic polarizability was quantitatively derived via the empirical additivity rule of ionic polarizabilities first established by Shannon [35]: $\alpha D = 2\alpha(Sm^{3+}) + 3(1–x)\alpha(Zr^{4+}) + 1.5x\alpha(Cr^{3+}) + 1.5x\alpha(Ta^{5+}) + 9\alpha(Mo^{6+}) + 36\alpha(O^{2-})$. According to the original work reported by Shannon, $\alpha(Sm^{3+}) = 4.74$ Å^3, $\alpha(Zr^{4+}) = 3.25$ Å^3, $\alpha(Cr^{3+}) = 1.45$ Å^3, $\alpha(Ta^{5+}) = 4.73$ Å^3, $\alpha(Mo^{6+}) = 3.28$ Å^3, and $\alpha(O^{2-}) = 2.01$ Å^3. From the perspective of solid dielectric physics, the Clausius–Mossotti relation is introduced to quantitatively correlate the macroscopic permittivity response of the as-sintered ceramics with the microscopic ionic polarization behavior of the cation-substituted crystal lattice [36]:

$$\alpha_{mea.}=\frac{V_{ce}(\varepsilon_r-1)}{Zb(\varepsilon_r+2)} \quad (7)$$

Taking the Lorentz local field shape factor $b=4\pi/3$ and the number of formula units per unit cell $Z=6$, the theoretical polarizability αth derived from the aforementioned polarizability calculation formulas and the experimental polarizability αmeainversely deduced from the measured dielectric parameters are all summarized in Table 3. The calculation results demonstrate that the numerical deviation between αth and αmeafalls within an acceptable range, and the minor discrepancy between them primarily originates from the inherent sensitivity of the Clausius–Mossotti model to the input empirical parameters [37].

Further comparison of the compositional evolution reveals that when the doping content of $(Cr_{0.5}Ta_{0.5})^{4+}$ increases from 0.02 to 0.11, the theoretical polarizability αth only slightly decreases from 726.6024 Å³ to 726.3432 Å³ (Table 3), with a variation amplitude less than 0.04%. However, the corresponding measured relative permittivity εr drops significantly from 10.52 to 7.23, reaching a reduction rate of 31.3%. This obvious difference in variation magnitude indicates that while intrinsic ionic polarizability establishes the baseline permittivity, the bulk density (i.e., porosity level) and chemical bond ionicity serve as the primary factors driving the sharp decline of εr with increasing substitution.

Generally, the main factors that affect the Q×f value of a ceramic sample include packing fraction (P.f), relative density, bond lattice energy (U), pores, lattice defects, and grain boundary scattering [32]. Fig. 7(c) details the variation in the Q×f value of the samples as a function of sintering temperature, showing that the maximum Q×f value of 72,764 GHz is achieved at the optimal sintering temperature of 800 °C for x = 0.02, while the dielectric properties for other doping points sintered at 800 °C are recorded in Table 3 and Table 5. Fig. 9(c) illustrates the correlation between the dielectric constant, packing fraction, and theoretical polarizability per unit volume (αtheo/Vm). The packing fraction, as an internal structural parameter, can be calculated using Equation (8) [38, 39]:

$$P.f=\frac{(\text{volume of ions in the cell})\times Z}{\text{volume of unit cell}}\times 100\% \quad (8)$$

Table 3 and Fig. 9(c) reveal that the packing fraction varies between 54.0% and 54.6% across the composition series. Within the x range of 0.02 to 0.11, the dramatic decline of Q×f from 72,764 GHz to 13,417 GHz cannot be attributed solely to the packing fraction, but is strongly coupled with the decrease in relative density (from 96.82% to 84.85%) and the intensified phonon scattering induced by local lattice distortion, as corroborated by Raman analysis.

This indicates that within the range of $0.02 \leq x \leq 0.11$, relative density and phonon damping act as the dominant extrinsic and intrinsic factors, respectively, in dictating the Q×f value. The modulation effect of relative density on Q×f can be

quantitatively understood through its close correlation with dielectric loss tangent (tanδ) and porosity (P = 1 – ρrelative) via Equation (9) and Equation (10) [18]:

$$\tan\delta=(1\text{-}P)\tan\delta_0+AP\left(\frac{P}{1\text{-}P}\right)^{2/3} \quad (9)$$

$$Q=\frac{1}{\tan\delta}\approx\frac{\omega^2{}_T}{\gamma\omega}=\frac{\omega^2{}_T}{2\pi\gamma f} \quad (10)$$

In Equation (9), $\tan\delta_0$ represents the intrinsic dielectric loss in pore-free conditions, tanδ represents the measured dielectric loss of the sample, and A' is a characteristic constant. Equation (10) describes the relationship between the Q×f value and the damping factor (γ), where ωT and γ represent the natural frequency and phonon damping coefficient of the ceramic, respectively [40]. When the porosity decreases, the pore fraction in the material is reduced, leading to an increase in relative density, which directly mitigates extrinsic dielectric loss and results in an improvement in the Q×f value. Therefore, the inverse relationship between porosity and Q×f faithfully reflects the dominant positive impact of densification on microwave dielectric performance.

The temperature coefficient of resonant frequency (τf) is a crucial parameter evaluating the thermal stability of microwave dielectric ceramics. As shown in Fig. 7(d) and Table 3, the τf values of the samples sintered at 800 °C vary from –32.59 ppm/°C to –27.26 ppm/°C across the substitution series (x = 0.02–0.11), exhibiting a slight minimum of –43.08 ppm/°C at x = 0.05. Generally speaking, τf is intrinsically governed by the crystal structure, linear thermal expansion coefficient (αL), and temperature coefficient of dielectric constant (τε), which can be well interpreted through bond valence theory and P-V-L bond energy analysis [24, 41]. The bond valence parameters can be expressed by equations (11) and (12) [40]:

$$V_i=\sum_j V_{ij} \quad (11)$$

$$V_{ij}=\mathrm{e}^{\left(\frac{R_{ij}-d_{ij}}{b}\right)} \quad (12)$$

In the equation, Rij represents the empirical bond valence parameter [38], and dij

represents the bond length of the chemical bond obtained through Rietveld refinement of XRD data, both recorded in Table 4, with the empirical constant b = 0.37 Å. The relationship between the chemical bond parameters and τf indicates that higher Mo–O bond strength effectively suppresses thermal expansion and anharmonic vibrations, thereby shifting τf toward zero [42].

Table 4 Bond length of the $Sm_2[Zr_{1-x}(Cr_{0.5}Ta_{0.5})_x]_3[MoO_4]_9$ ceramics selected at optimal sintering temperatures.

Bonds	**x=0.02**	**x=0.05**	**x=0.08**	**x=0.11**
Sm-O(1)¹	2.436	2.433	2.461	2.462
Sm-O(1)²	2.436	2.434	2.462	2.462
Sm-O(1)³	2.435	2.433	2.461	2.461
Sm-O(2)¹	2.415	2.404	2.490	2.403
Sm-O(2)²	2.416	2.404	2.490	2.403
Sm-O(2)³	2.416	2.404	2.490	2.403
Sm-O(6)¹	2.582	2.518	2.520	2.586
Sm-O(6)²	2.582	2.518	2.520	2.586
Sm-O(6)³	2.582	2.518	2.521	2.586
Zr($Cr_{0.5}Ta_{0.5}$)1-O(4)×6	2.043	2.055	2.099	2.065
Zr($Cr_{0.5}Ta_{0.5}$)2-O(3)¹	2.132	2.165	2.147	2.147
Zr($Cr_{0.5}Ta_{0.5}$)2-O(3)²	2.133	2.166	2.148	2.147
Zr($Cr_{0.5}Ta_{0.5}$)2-O(3)³	2.132	2.166	2.147	2.147
Zr($Cr_{0.5}Ta_{0.5}$)2-O(5)¹	2.038	1.995	1.992	1.911
Zr($Cr_{0.5}Ta_{0.5}$)2-O(5)²	2.038	1.995	1.992	1.911
Zr($Cr_{0.5}Ta_{0.5}$)2-O(5)³	2.039	1.995	1.993	1.912
Mo1-O(1)	1.696	1.688	1.654	1.640
Mo1-O(2)	1.762	1.778	1.698	1.756
Mo1-O(3)	1.780	1.723	1.739	1.733
Mo1-O(4)	1.829	1.791	1.752	1.801
Mo2-O(5)1	1.832	1.863	1.869	1.875
Mo2-O(5)2	1.832	1.863	1.869	1.875
Mo2-O(6)×2	1.604	1.676	1.667	1.596

Average Sm-O	2.4778	2.4518	2.4906	2.4836
Average Zr1-O	2.0430	2.0550	2.0990	2.0650
Average Zr2-O	2.0853	2.0803	2.0698	2.0292
Average Mo1-O	1.7668	1.7450	1.7107	1.7325
Average Mo2-O	1.7180	1.7695	1.7680	1.7355

3.4 Chemical Bond Analysis Based on the P–V–L Model

This study demonstrates that the crystal structural configuration exerts a dominant modulation effect on the performance of the as-prepared microwave dielectric ceramics. A series of key chemical bond parameters, namely bond ionicity (fi), lattice energy (U), bond energy (E) and linear thermal expansion coefficient (αmn), are precisely determined by performing Rietveld refinement on the collected XRD patterns, with all detailed data tabulated in Table 3 and Table 4. According to the P-V-L chemical bond theory, the complex chemical bonds in the $Sm_2[Zr_{1-x}(Cr_{0.5}Ta_{0.5})_x]_3[MoO_4]_9$ system are decomposed into the sum of binary AmBn sub-crystals, following the methodology reported in Refs. [41, 42].

$$\begin{aligned} &Sm_2[Zr_{1-x}(Cr_{0.5}Ta_{0.5})_x]_3[MoO_4]_9 \\ \rightarrow &Sm_2(10)+Zr/(Cr_{0.5}Ta_{0.5})(9)+Zr/(Cr_{0.5}Ta_{0.5})(11)_2+Mo(1)_6 \\ &+Mo(8)_3+O(2)_6+O(3)_6+O(4)_6+O(5)_6+O(6)_6+O(7)_6 \\ &\rightarrow Sm_{2/3}O(1)_3+Sm_{2/3}O(2)_3+Sm_{2/3}O(6)_3 \\ &+Zr/(Cr_{0.5}Ta_{0.5})(9)O(2)_3+Zr/(Cr_{0.5}Ta_{0.5})(11)O(3)_3+Zr/(Cr_{0.5}Ta_{0.5})(9)O(6)_3 \\ &+Mo(1)_{3/2}O(2)_3+Mo(1)_{3/2}O(3)_3+Mo(1)_{3/2}O(4)_3 \\ &+Mo(1)_{3/2}O(7)_3+Mo(8)_{3/2}O(5)_3+Mo(8)_{3/2}O(6)_3 \end{aligned} \quad (13)$$

In this study, the formal effective valence states of cations residing at inequivalent Wyckoff crystallographic sites are systematically verified: the Sm^{3+}-occupied lattice sites maintain a stable +3 valence, the $Zr/(Cr_{0.5}Ta_{0.5})$ mixed-occupancy coordination sites exhibit an averaged +4 nominal valence, and the Mo^{6+}-centered polyhedra are confirmed to retain the +6 valence state throughout the entire doping series. Meanwhile, the oxygen anions distributed in three distinct coordination polyhedral frameworks (Sm-O, $Zr/(Cr_{0.5}Ta_{0.5})$-O and Mo-O) are assigned with unique fractional effective valence values of -2/3, -4/3 and -3, respectively.

From the viewpoint of solid-state physical chemistry, the macroscopic dielectric permittivity of sintered polycrystalline dielectrics is intrinsically governed by the total ionic polarizability of constituent structural units, which exhibits a well-defined positive correlation with the ionic contribution fraction of individual chemical bonds. This underlying physical nature establishes an unambiguous causal linkage between the bond ionicity and measured permittivity, implying that the compositional evolution of bond ionicity will impose a direct regulatory effect on the dielectric constant of the ceramic matrix. The explicit mathematical formulation describing this quantitative correlation is documented in Ref. [42]:

$$\varepsilon_r=\frac{n^2-1}{1-f_i}+1 \tag{14}$$

$$f_i^{\mu}=\frac{(C)^2}{(E_g)^2} \tag{15}$$

$$(E_g)^2=(E_h)^2+(C)^2 \tag{16}$$

$$(E_h)^2=\frac{39.74}{(d)^{2.48}} \tag{17}$$

$$C=\frac{14.4b\exp(-K_s d/2)\left[(Z_A)^*-\frac{n}{m}(Z_B)^*\right]}{2} \tag{18}$$

Within the P-V-L chemical bond theoretical framework employed in the present study, the symbol nn denotes the refractive index, while Eh, C and Eg are rigorously defined as the homopolar polarization energy, heteropolar polarization energy, and averaged total energy gap, respectively. The rest of the involved parameters are specified as follows: d refers to the interatomic chemical bond length, b represents the empirical correction coefficient, exp(-Ksd/2) corresponds to the Thomas–Fermi screening factor, and Z_A^* , Z_B^* stand for the effective valence electron numbers of the cation and anion in each binary sub-crystal.

As shown in Fig. 8(a), the average bond ionicity of Sm–O, (Cr/Ta)–O, and Mo–O bonds exhibits a distinct hierarchical distribution, strictly following the order Ave fi(Sm–O) > Ave fi((Cr/Ta)–O) > Ave fi(Mo–O). This result demonstrates that the ionic character of Sm–O bonds plays a substantial role in lattice polarization. Fig. 9(a, b)

and Fig. 7(b) further present the correspondence between chemical bond ionicity and measured ε_r values. From the perspective of solid-state dielectric physics, the dielectric constant measures the material's ability to store electric polarization, which is intrinsically tied to bond ionicity and polarizability. As the substitution level increases, the slight decline in bond ionicity together with the decrease in densification drives the overall reduction in permittivity.

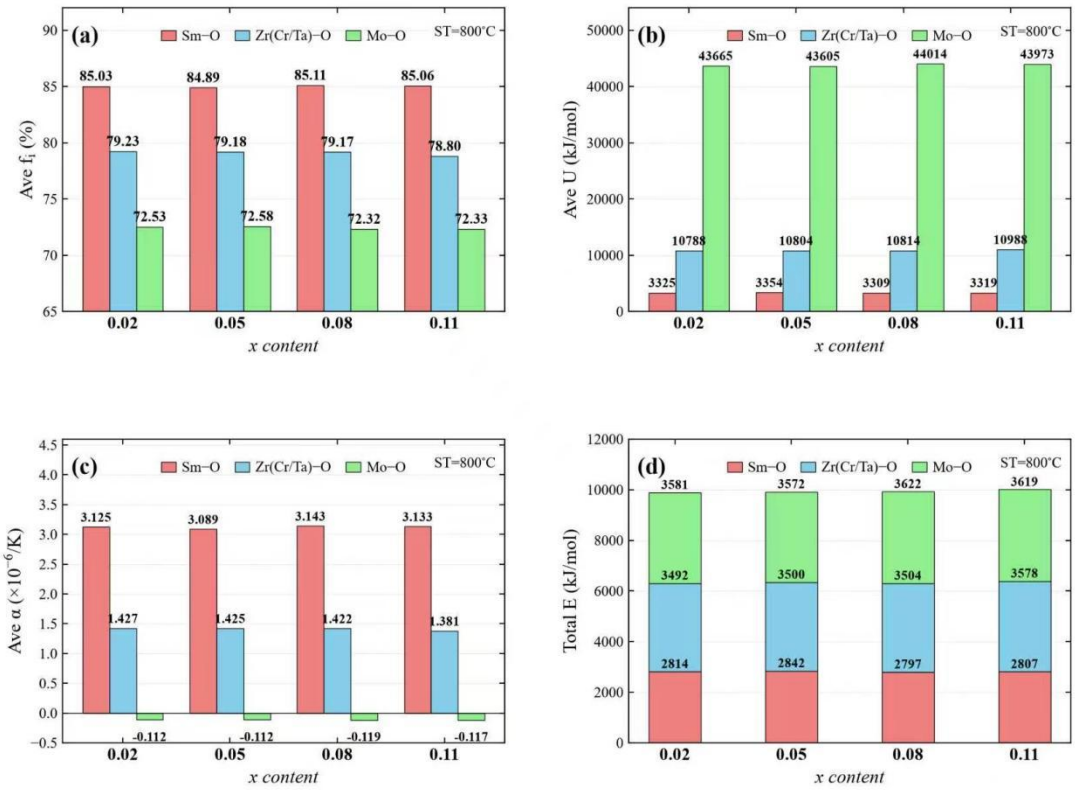


Fig. 8. Calculated chemical bond parameters of $Sm_2[Zr_{1-x}(Cr_{0.5}Ta_{0.5})_x]_3[MoO_4]_9$ ceramics sintered at 800 °C: (a) average bond ionicity (fi), (b) average lattice energy (Ub), (c) average linear thermal expansion coefficient (αmn), and (d) total bond energy (E).

The concept of lattice energy provides a quantitative assessment of the net cohesive forces operating among ionic constituents within a crystal. An elevated lattice energy correlates directly with superior lattice rigidity, thereby imposing a higher activation barrier for thermally or field-induced vibrational excitations. This constrained vibrational behavior consequently mitigates the energy dissipation attributable to the anharmonic motion of ions under time-varying electric fields. The

specific computational procedure for lattice energy, rooted in the P-V-L framework, is explicitly provided by the subsequent equation, as referenced from Ref [43]:

$$U_b^{\mu}=U_{bc}^{\mu}+U_{bi}^{\mu} \tag{19}$$

$$U_{bc}^{\mu}=2100m\frac{\left(Q_A^{\mu}\right)^{1.64}}{\left(d^{\mu}\right)^{0.75}}f_c^{\mu} \tag{20}$$

$$U_{bi}^{\mu}=1270\frac{(m+n)Z_A^{\mu}Z_B^{\mu}}{d^{\mu}}\left(1-\frac{0.4}{d^{\mu}}\right)f_i^{\mu} \tag{21}$$

In the equation, Ubc corresponds to the covalent component of the chemical bond lattice energy in the dielectric ceramic, while Ubi represents its ionic component. Z+ and Z− denote the valences of the positive and negative ions in the chemical bond, respectively. As can be observed from Fig. 8(b), Ave U(Mo–O) > Ave U(Zr/($Cr_{0.5}Ta_{0.5}$)–O) > Ave U(Sm–O), indicating that the Mo–O bond possesses the highest lattice energy and dominates the overall lattice rigidity of the ceramic matrix. Bond energy and linear expansion coefficient are both critical parameters that dictate the τf of the sample. The expression for bond energy is [44, 45]:

$$E=E_c+E_i \tag{22}$$

$$t_i=\left|\frac{(S_A-S_B)}{6}\right| \tag{23}$$

$$t_c+t_i=1 \tag{24}$$

$$Ei = 14.4\ ti / d \tag{25}$$

$$E_c=\frac{(r_{CA}+r_{CB})}{d}(E_{A\text{-}A}E_{B\text{-}B})^{1/2} \tag{26}$$

Within the P-V-L chemical bond theory framework, Ec and Ei are defined as the energy contributions originating from the covalent and ionic components of a single chemical bond, respectively. Herein, SA and SB correspond to the Pauling electronegativities of element A and element B, rCA and rCB refer to the covalent radii of the two bonding atoms, while EA-A denotes the homonuclear bond dissociation energy retrieved from standard handbooks [46]. Fig. 8(d) systematically visualizes the average bond energy contributions of three typical coordination bonds

(Sm–O, Mo–O, (Cr/Ta)–O) in the $Sm_2[Zr_{1-x}(Cr_{0.5}Ta_{0.5})_x]_3[MoO_4]_9$ ceramic system, as well as their respective weight proportions in the total system bond energy.

Notably, the Mo–O bond exhibits the maximum bond energy among all detected coordination species, which strongly indicates that the Mo–O bonding interaction dominates the modulation effect on the temperature coefficient of resonant frequency (τf) of the as-prepared ceramics. Fig. 8(c) summarizes the averaged linear thermal expansion coefficients of different chemical bonds in the $Sm_2[Zr_{1-x}(Cr_{0.5}Ta_{0.5})_x]_3[MoO_4]_9$ system. The linear thermal expansion coefficient of Mo–O bond approaches near-zero values, verifying that the linear expansion behavior of Mo–O bonds plays a leading role in determining the final τf performance. The intrinsic relationship between τf and αmn can be mathematically described by equations (27)–(31) [41, 42]:

$$\tau_f = -\left(\frac{\tau_\varepsilon}{2} + \alpha_L\right) \quad (27)$$

$$\beta_{mn} = \frac{m(m+n)}{2n} \quad (28)$$

$$\gamma_{mn} = \frac{kZ_A N_{CA}}{U_b \Delta_A} \beta_{mn} \quad (29)$$

$$\alpha_{mn} = -3.1685 + 0.8376\gamma_{mn} \quad (30)$$

$$\alpha_L = \sum F_{mn}\alpha_{mn} \quad (31)$$

Within the theoretical analysis framework of dielectric properties, N_{CA} is defined as the coordination number of cations, τ_ε refers to the temperature coefficient of dielectric permittivity, k represents the Boltzmann constant, △A denotes the periodic characteristic constant of cations, and Fmn corresponds to the occupancy proportion of a single type of chemical bond in the system. The linear thermal expansion coefficient of chemical bonds characterizes the variation law of bond length when the material temperature fluctuates, and the temperature coefficient of this parameter is intrinsically correlated with the thermal stability of the as-prepared ceramics.

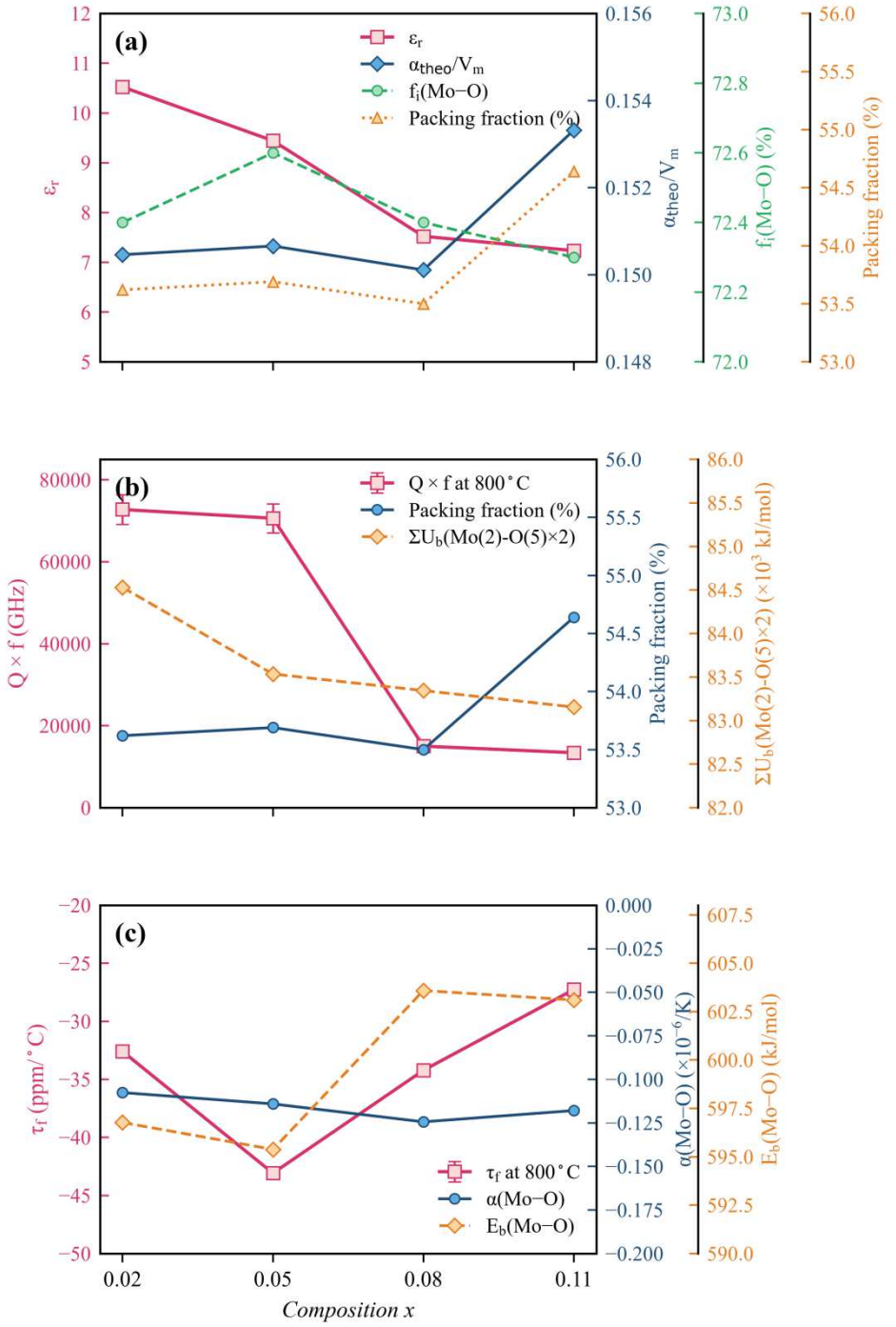


Fig. 9. Correlations between structural/bond parameters and dielectric properties for $Sm_2[Zr_{1-x}(Cr_{0.5}Ta_{0.5})_x]_3[MoO_4]_9$ ceramics sintered at 800 °C: (a) bond ionicity and theoretical polarizability, (b) permittivity and Mo–O bond ionicity, and (c) permittivity, packing fraction, and polarizability per unit volume.

3.5 Raman Spectroscopy Analysis

Figure 10(a) presents the Raman spectra of $Sm_2[Zr_{1-x}(Cr_{0.5}Ta_{0.5})_x]_3[MoO_4]_9$ ceramics with doping contents ranging from x = 0.02 to x = 0.11. All characteristic peaks are in perfect agreement with the spectral signatures of the rhombohedral R3c space group, which definitively verifies the successful formation of homogeneous single-phase solid solutions across the entire investigated doping range. The detected vibrational modes can be primarily assigned to the internal stretching and bending vibrations of $[MoO_4]$ tetrahedral units, as well as the external lattice vibrations associated with the framework Sm^{3+} rare-earth cations.

An anomalous phenomenon is observed in this system: the Raman peaks first shift to higher wavenumbers and then reversely move to lower wavenumbers, while the dielectric permittivity maintains a monotonous downward trend throughout the whole doping interval. This counterintuitive behavior can be rationally elucidated by a multi-stage coupling mechanism of microstructure evolution, whose core physical essence lies in the sequential dominance of distinct structural factors, which collectively induce the continuous attenuation of the macroscopic polarization capability of the system. In the first low-doping stage where Raman blue-shift and permittivity decrease occur synchronously, the Raman blue-shift is governed by the enhanced local compressive stress and the elevated chemical bond force constant k. After low-concentration dopant atoms are incorporated into the lattice, they preferentially trigger local lattice compression, shorten interatomic distances and improve bond strength. According to the diatomic harmonic vibration model, the characteristic lattice vibration frequency increases correspondingly, driving the Raman characteristic peaks to shift towards higher wavenumbers. The physical origin of the synchronous permittivity reduction in this stage is that the lattice densification during compression remarkably suppresses the concentration of polarizable defect dipoles (e.g., oxygen-vacancy-related dipole pairs), while the elevated bond strength directly reduces the intrinsic lattice polarizability. Macroscopically, this manifests as a continuous decline of permittivity with increasing doping content, which is fully consistent with the Raman blue-shift process.

When the doping concentration exceeds the critical threshold and enters the second stage, the dominant structural factor of the system switches completely: the pre-existing local compressive stress is fully counteracted by massive newly generated lattice tensile strain, non-equilibrium oxygen vacancies and local lattice disorder. The chemical bonds are elongated, the bond strength is significantly weakened, the chemical bond force constant k decreases synchronously, the characteristic lattice vibration frequency reduces, and consequently the Raman characteristic peaks shift towards lower wavenumbers. The core logic for the persistent permittivity decrease in this stage is that although the moving direction of Raman peaks is reversed, the total polarization capability of the system — the core physical quantity that determines permittivity — still keeps attenuating. A large number of non-equilibrium oxygen vacancies form stable defect clusters in the lattice, which further trap the originally freely migrating defect dipoles, and the substantially elevated local lattice disorder further reduces the overall system polarizability. As a result, the permittivity does not rebound with the reversal of Raman peak shift direction, but maintains a stable monotonous downward trend all along. In addition, the relative density also decreases with the increase of doping content, which makes the variation trend of permittivity highly consistent with the evolution law of relative density and the Raman spectral characteristics.

Figure 10(b) provides a high-resolution visualization of the Raman spectra for $Sm_2[Zr_{1-x}(Cr_{0.5}Ta_{0.5})_x]_3[MoO_4]_9$ ceramics, which is processed via peak deconvolution using a Gauss-Lorentz hybrid function. The "Experimental" curve corresponds to the raw measured Raman spectral dataset, while the "Fitted" curve is derived from the full-profile fitting procedure based on the Gauss-Lorentz crossover function. This post-processing approach effectively resolves overlapping characteristic peaks and accurately identifies the specific vibrational modes of the target material, delivering critical structural information for establishing the correlation between crystal structure evolution and macroscopic dielectric properties.

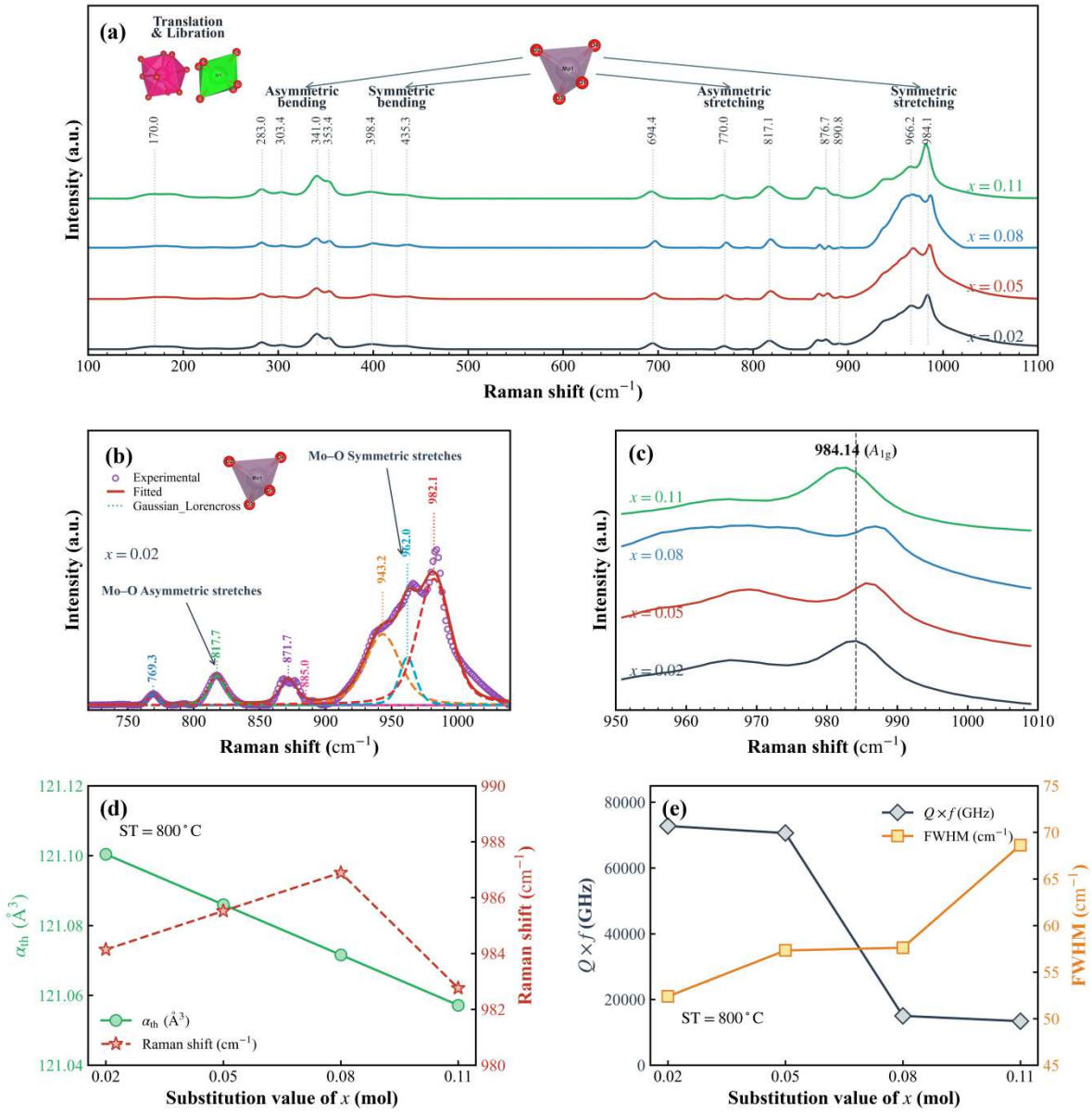


Fig. 10. Raman spectroscopy analysis of $Sm_2[Zr_{1-x}(Cr_{0.5}Ta_{0.5})_x]_3[MoO_4]_9$ ceramics sintered at 800 °C: (a) stacked Raman spectra in the range of 100–1100 cm^{-1}; (b) Gaussian-Lorentzian deconvolution in the 720–1040 cm^{-1} region for x = 0.02; (c) magnified view of the A_{1g} mode shift; (d) theoretical polarizability (αth) and Raman shift of A_{1g} mode; (e) microwave quality factor (Q×f) and Raman FWHM as a function of substitution content x.

Further referencing the research foundation of rare-earth molybdate structural spectroscopy, the distinct Raman signal centered near 984–987 cm^{-1} can be unambiguously assigned to the characteristic A_{1g} symmetric stretching mode of the $[MoO_4]$ tetrahedral unit [25, 46]. To clearly capture its subtle evolutionary law, the locally magnified spectrum of this A_{1g} mode is presented in Fig. 10(c), which

demonstrates the peak position shifting with increasing $(Cr_{0.5}Ta_{0.5})^{4+}$ substitution level (Table 5). This structural evolution reflects changes in the local coordination field and force constant of Mo–O bonds, which can be correlated with the polarization behavior.

$$\frac{\varepsilon_r-1}{\varepsilon_r+2}=\frac{N(\alpha_e+\alpha_d+\frac{\mu^2}{3KT})}{3\varepsilon_0} \quad (32)$$

Herein, αe and αd are defined as the electronic polarizability and the dipolar/vibrational polarizability of the system, respectively. The evolutionary trend of the Raman peak position reflects the modification of local bonding symmetry and force constants in the as-prepared samples, correlating with the polarizability trends shown in Fig. 10(d) and Table 5.

Table 5 Summary of Raman spectroscopy data (A_1g mode shift and FWHM), theoretical polarizability (α_{th}), relative permittivity (ε_r), and microwave quality factor (Q×f) for $Sm_2[Zr_{1-x}(Cr_{0.5}Ta_{0.5})_x]_3[MoO_4]_9$ (x = 0.02–0.11) ceramics sintered at 800 °C.

Composition (x)	ST (°C)	Raman shift of A_1g (cm^{-1})	αth (Å³) [per f.u.]	αth (Å³) [per cell, Z=6]	Q × f (GHz)	FWHM of A_1g (cm^{-1})	εr	τf (ppm/°C)
0.02	800	984.14	121.1004	726.6024	72,764	52.39	10.52	-32.59
0.05	800	985.52	121.0860	726.5160	70,624	57.32	9.44	-43.08
0.08	800	986.89	121.0716	726.4296	15,016	57.62	7.52	-34.22
0.11	800	982.76	121.0572	726.3432	13,417	68.62	7.23	-27.26

To systematically clarify the intrinsic correlation between the full width at half maximum (FWHM) of the characteristic Raman peak and the quality factor Q×f, Fig. 10(e) plots the synchronous evolution of the FWHM of the A_1g mode and the Q×f value of the corresponding sample as a function of doping concentration x. The specific numerical datasets for these parameters are summarized in Table 5. The quantitative mathematical expression describing the inherent relationship between the Raman FWHM and dielectric damping is given as follows:

$$FWHM=\frac{\gamma\sqrt{\gamma^2+4W_0^2}}{2W_0^2} \quad (33)$$

Herein, γ denotes the lattice phonon damping coefficient, while W_0 corresponds to the central resonant frequency of the target phonon mode. Derived from the combined relationships, the full width at half maximum (FWHM) of the Raman peak exhibits an inverse correlation with the quality factor Q×f, which is in excellent agreement with the experimental trend visualized in Fig. 10(e). As x increases from 0.02 to 0.11, the FWHM broadens from 52.39 cm^{-1} to 68.62 cm^{-1}, reflecting intensified lattice anharmonicity and phonon scattering, which directly drives the degradation of Q×f from 72,764 GHz to 13,417 GHz. This confirms that intrinsic phonon damping is the primary physical mechanism governing the dielectric loss in this ceramic system.

4. Conclusion

A remarkable enhancement in quality factor (Q×f) was realized in $Sm_2[Zr_{1-x}(Cr_{0.5}Ta_{0.5})_x]_3[MoO_4]_9$ ceramics via strategic B-site co-substitution and low-temperature sintering. The composition with x = 0.02, sintered at 800 °C, demonstrated superior microwave dielectric performance: a permittivity (ε_r) of 10.52, an ultra-high Q×f value of 72,764 GHz, and a temperature coefficient of resonant frequency (τf) of –32.59 ppm/°C. The exceptional Q×f improvement is primarily attributed to the reinforcement of intrinsic lattice stability, with densification playing a secondary role. The introduction of Zr^{4+} facilitates densification at lower temperatures, while the increased Mo–O lattice energy and diminished phonon scattering, as indicated by the narrowing of Raman peak full width at half maximum (FWHM), synergistically suppress dielectric loss. Furthermore, the lower ionic polarizability of Sm^{3+} contributes to mitigating local structural distortion. These findings highlight the promising potential of B-site engineered molybdate ceramics for developing next-generation, low-loss, and thermally stable microwave components.

Data availability

The data that support the findings of this study are openly available to the reviewers.

Declarations

Conflict of interest The authors declare that they have no known competing financial interests or personal relationships that could have appeared to influence the work reported in this paper.

Acknowledgments

This work was financially supported by 20252112 Scientific Research Startup Fund for Introduced Talents of Taiyuan University of Science and Technology.

References

[1] T.S. Rappaport, S. Sun, R. Mayzus, H. Zhao, Y. Azar, K. Wang, G.N. Wong, J.K. Schulz, M. Samimi, F. Gutierrez, Millimeter wave mobile communications for 5G cellular: It will work!, IEEE Access 1 (2013) 335–349.

[2] O. Elijah, C.Y. Leow, T.A. Rahman, S. Nunoo, S.Z. Iliya, A comprehensive survey of pilot contamination in massive MIMO—5G system, IEEE Commun. Surv. Tutor. 18 (2016) 905–923.

[3] A. Roy, A. Sen, Microwave dielectric properties of $CaCu_3Ti_4O_{12}$ ceramics: A clue to its intrinsic dielectric response, J. Adv. Dielect. 13 (2023) 2350011.

[4] C.-G. Gheorghe, L. Gheorghe, I. Ungurean, N. Bizon, Latency requirement for 5G mobile communications, in: Proc. 10th Int. Conf. Electron. Comput. Artif. Intell. (ECAI), 2018, pp. 1–4.

[5] J. Yao, S. Tjuatja, H.-Y. Hwang, J. Ko, Far-field interrogation of microstrip patch antenna for temperature sensing without electronics, IEEE Sens. J. 16 (2016) 7053–7060.

[6] B. Masin, J. Varghese, M.T. Sebastian, Temperature-compensated BaV_2O_6-$Ba_2V_2O_7$ ceramic composite for ULTCC applications, Ceram. Int. 48 (2022) 22479–22485.

[7] W.J. Guo, X.K. Lan, Z.X. Fu, P. Liu, Structure, defects, and microwave dielectric properties of Al-doped and Al/Nd co-doped $Ba_4Nd_{9.33}Ti_{18}O_{54}$ ceramics, J. Adv. Ceram. 11 (2022) 629–640.

[8] Y. Tang, L. Luo, Y. Li, Q. Zhao, T. Yang, T. Yang, T. Tang, Tuning the order-disorder of $Zn_{2-2x}Li_xGa_{4+x}O_8$ spinel towards high-performance microwave dielectric ceramic, J. Alloys Compd. 927 (2022) 167026.

[9] H. Pan, F. Huang, X. Wu, X. Tang, Q. Zhang, Composition-structure-property relationships in $CeZr_{1.14}Bi_{0.045}A_{0.045}Mo_{4.5}O_{18}$ (A = Nb, Ta, Sb) microwave dielectric ceramics revealed by Raman, far-infrared and terahertz spectra, J. Mater. Res. Technol. 25 (2023) 369–381.

[10] J. Bao, Y. Yuan, Y. Zhang, Y. Yang, Crystal structure, Raman spectrum, bond characteristics, and terahertz time-domain spectrum of novel $Na_5Tm(MoO_4)_4$ microwave dielectric ceramic with ultra-low sintering temperature and high quality factor, J. Alloys Compd. 939 (2023) 168652.

[11] D. Johnson, M.T. Sebastian, R. Ubic, Synthesis and characterization of $Na_5M(MoO_4)_4$ (M = Y, Yb) microwave ceramics for ULTCC applications, Ceram. Int. 44 (2018) 6699–6704.

[12] Y.B. Chen, S. Xiong, Raman spectra and microwave dielectric properties of $Na_5Tm_{1-x}(Y_{1/3}Yb_{2/3})_x(MoO_4)_4$ ceramics with ultra-low sintering temperature, Sci. Rep. 15 (2025) 6644.

[13] N. Joseph, M.T. Sebastian, Glass-free $CuMoO_4$ ceramic with excellent dielectric and thermal properties for ultralow temperature cofired ceramic applications, ACS Sustain. Chem. Eng. 4 (2016) 5632–5639.

[14] X. Lyu, L. Li, J. Li, W. Zhang, Sintering behavior, structure, and microwave properties of novel $Li_{2x}Cu_{1-x}MoO_4$ ceramics, Ceram. Int. 48 (2022) 17225–17233.

[15] L. Ren, J. Li, W. Zhang, W^{6+} doped $CuMoO_4$ ceramics with low dielectric permittivity and near-zero temperature coefficient of resonant frequency for ULTCC application, J. Eur. Ceram. Soc. 45 (2025) 116986.

[16] W. Liu, R. Zuo, Low temperature fired $Ln_2Zr_3(MoO_4)_9$ (Ln = Sm, Nd) microwave dielectric ceramics, Ceram. Int. 43 (2017) 17229–17232.

[17] Y. Jiang, X. Lu, C. Li, Sintering behavior, infrared spectra and microwave dielectric characteristics analysis for $Ce_2Zr_3(MoO_4)_9$ ceramics achieved by reaction-sintering method, J. Alloys Compd. 875 (2021) 160096.

[18] C. Xing, H. Wu, Y. Chen, Crystal structure, infrared spectra and microwave dielectric properties of low-firing $La_2Zr_3(MoO_4)_9$ ceramics prepared by reaction-sintering process, Ceram. Int. 45 (2019)

22376–22382.
[19] Y.H. Zhang, L. Li, J. Bao, Crystal structure, infrared spectra and microwave dielectric properties of novel extra-low temperature fired $Eu_2Zr_3(MoO_4)_9$ ceramics, J. Eur. Ceram. Soc. 39 (2019) 1127–1131.
[20] J. Zheng, X. Wu, Y. Tang, Structure, infrared reflectivity spectra and microwave dielectric properties of a low-firing microwave dielectric ceramic $Pr_2Zr_3(MoO_4)_9$, J. Alloys Compd. 826 (2020) 153893.
[21] C.F. Xing, Y. Li, H. Pan, Crystal structure, infrared spectra and microwave dielectric properties of a novel low-firing $Gd_2Zr_3(MoO_4)_9$ ceramic, Ceram. Int. 45 (2019) 22207–22214.
[22] X. Zhou, L. Liu, J. Sun, N. Zhang, H. Sun, H. Wu, W. Tao, Effects of $(Mg_{1/3}Sb_{2/3})^{4+}$ substitution on the structure and microwave dielectric properties of $Ce_2Zr_3(MoO_4)_9$ ceramics, J. Adv. Ceram. 10 (2021) 778–789.
[23] Y. Chen, H. Li, X. Xu, Y. Zhang, J. Du, H. Wu, L. Liu, G. Duan, Effects of $(Ba_{1/3}Sb_{2/3})^{4+}$ on the structure and dielectric properties of $Ce_2Zr_3(MoO_4)_9$ ceramic at microwave frequency, J. Alloys Compd. 939 (2023) 168804.
[24] H. Pan, F. Huang, X. Wu, Significant improvement on quality factor in Bi^{3+}/Ta^{5+} codoped $Ce_2Zr_{3-3x}Bi_{1.5x}Ta_{1.5x}Mo_9O_{36}$ microwave dielectric ceramics with ultra-low sintering temperatures, Ceram. Int. 49 (2023) 32979–32988.
[25] C. Feng, X. Zhou, B. Tao, H. Wu, S. Huang, Crystal structure and enhanced microwave dielectric properties of the $Ce_2[Zr_{1-x}(Al_{1/2}Ta_{1/2})_x]_3(MoO_4)_9$ ceramics at microwave frequency, J. Adv. Ceram. 11 (2022) 392–402.
[26] B.W. Hakki, P.D. Coleman, A dielectric resonator method of measuring inductive capacities in the millimeter range, IEEE Trans. Microw. Theory Tech. 8 (1960) 402–410.
[27] M. Zang, M. Zheng, M. Zhu, Y. Hou, Low-temperature sintering and microwave dielectric properties of $CaMoO_4$ ceramics for LTCC and ULTCC applications, J. Eur. Ceram. Soc. 44 (2024) 293–301.
[28] D. Xu, H. Zhang, L. Pang, F. Hussain, T. Zhou, S.-K. Sun, Z. Chen, D. Zhou, Novel B-site scheelite structure ceramic $Bi(Ge_{0.5}Mo_{0.5})O_4$ and its dielectric properties, J. Am. Ceram. Soc. 106 (2023) 6675–6683.
[29] Y. Li, D. Liang, X. Zhang, Z. Xiong, B. Tang, F. Si, Z. Fang, Z. Shi, J. Chen, F. Wang, H. Li, Sintering behavior, crystal structure, and microwave dielectric properties of a novel $NaY_9Si_6O_{26}$ ceramic, J. Am. Ceram. Soc. 107 (2024) 4077–4085.
[30] G. Gouadec, P. Colomban, Raman spectroscopy of nanomaterials: how spectra relate to disorder, particle size and mechanical properties, Prog. Cryst. Growth Charact. Mater. 53 (2007) 1–56.
[31] Y. Imanaka, Multilayered Low Temperature Cofired Ceramics (LTCC) Technology, Springer, New York, 2005.
[32] S.J. Penn, N.M. Alford, A. Templeton, X. Wang, M. Xu, M. Reece, K. Schrapel, Effect of porosity and grain size on the microwave dielectric properties of sintered alumina, J. Am. Ceram. Soc. 80 (1997) 1885–1888.
[33] L. Shi, C. Liu, H. Zhang, R. Peng, G. Wang, X. Shi, X. Wang, W. Wang, Crystal structure, Raman spectroscopy, metal compatibility and microwave dielectric properties of $Ce_2Zr_3(MoO_4)_9$ ceramics, Mater. Chem. Phys. 250 (2020) 122954.
[34] R. Gupta, E.Y. Kim, H.-S. Shin, G.-Y. Lee, D.-H. Yeo, Structural, microstructural, and microwave dielectric properties of $(Al_{1-x}B_x)_2Mo_3O_{12}$ ceramics with low dielectric constant and low dielectric loss

for LTCC applications, Ceram. Int. 49 (2023) 22690–22701.
[35] R.D. Shannon, Dielectric polarizabilities of ions in oxides and fluorides, J. Appl. Phys. 73 (1993) 348–366.
[36] M.-R. Joung, J.-S. Kim, M.-E. Song, S. Nahm, J.-H. Paik, B.-H. Choi, Formation and microwave dielectric properties of the $Mg_2V_2O_7$ ceramics, J. Am. Ceram. Soc. 92 (2009) 1621–1624.
[37] S. Liu, H. Li, R. Xiang, P. Zhang, X. Chen, Q. Wen, H. Hu, Effect of substituting Al^{3+} for Ti^{4+} on the microwave dielectric performance of $Mg_2Ti_{1-x}Al_{4/3x}O_4$ ($0.01 \leq x \leq 0.09$) ceramics, Ceram. Int. 47 (2021) 33064–33069.
[38] C.-H. Su, F.-C. Lin, T.-M. Chu, C.-L. Huang, Structural characteristics and microwave dielectric properties of low-firing $Ba(Co_{1-x}Mg_x)_2(VO_4)_2$ ($x = 0–1$) ceramics, J. Alloys Compd. 686 (2016) 608–615.
[39] Y. Zhang, H. Wu, Crystal structure and microwave dielectric properties of $La_2(Zr_{1-x}Ti_x)_3(MoO_4)_9$ ($0 \leq x \leq 0.1$) ceramics, J. Am. Ceram. Soc. 102 (2019) 4092–4102.
[40] K. Fukuda, R. Kitoh, I. Awai, Far-infrared reflection spectra of dielectric ceramics for microwave applications, J. Am. Ceram. Soc. 77 (1994) 149–154.
[41] S. Zhang, H. Li, S. Zhou, T. Pan, Estimation thermal expansion coefficient from lattice energy for inorganic crystals, Jpn. J. Appl. Phys. 45 (2006) 8801–8804.
[42] H. Tian, X. Liu, Y. Yang, H. Wu, Z. Zhang, Crystal structure, infrared spectra, and microwave dielectric properties of $Ce_2(Zr_{0.94}Sn_{0.06})_3(MoO_4)_9$ ceramics with low sintering temperature, Front. Mater. 7 (2020) 145.
[43] S.B. Stepan, Dielectric methods of studying the chemical bond and the concept of electronegativity, Russ. Chem. Rev. 51 (1982) 684–698.
[44] R.T. Sanderson, Electronegativity and bond energy, J. Am. Chem. Soc. 105 (1983) 2259–2261.
[45] Y.-B. Chen, S. Xiong, Structural characteristics, P-V-L theory, Raman spectra, and microwave dielectric properties of $(La_{1-x}Nd_x)_2(Zr_{0.96}Ti_{0.04})_3(MoO_4)_9$ ceramics for LTCC applications, J. Eur. Ceram. Soc. 45 (2025) 116974.
[46] Y.-R. Luo, Comprehensive Handbook of Chemical Bond Energies, 1st ed., CRC Press, Boca Raton, 2007.